RARE METALS

ORIGINAL ARTICLE

Chemical vapor deposition synthesis of V-doped MoS$_2$

Yang Yang, Qing-Rong Liang, Chun-Li Zhu* , **Guo-Zhong Zheng,
Jian Zhang, Shou-Jun Zheng, Yung-Chang Lin, De-Zhi Zheng,
Jia-Dong Zhou***

Abstract Van der Waals coupling with different stacking configurations can significantly affect the optical and electronic properties of ultrathin two-dimensional (2D) materials, which is an effective way to tune device performance. Herein, we report a salt-assisted chemical vapor deposition method for the synthesis of bilayer V-doped MoS$_2$ with 2H and 3R phases, which are demonstrated by the second harmonic generation and scanning transmission electron microscopy. Notably, the mobility of the 3R phase V-doped MoS$_2$ is 6.2% higher than that of the 2H phase. Through first-principles calculations, we further reveal that this particular behavior is attributed to the stronger interlayer coupling of 3R compared to the 2H stacking configuration. This research can be further generalized to other transition metal chalcogenides and will contribute to the development of electronic devices based on 2D materials in the future.

Keywords Chemical vapor deposition; Synthesis; First-principles calculations; 2H; 3R

Yang Yang and Qing-Rong Liang have contributed equally to this work.

Y. Yang, Q.-R. Liang, S.-J. Zheng, J.-D. Zhou*
School of Physics, Beijing Institute of Technology, Beijing 100081, China
e-mail: jdzhou@bit.edu.cn

C.-L. Zhu*
School of Information and Electronics and Advanced Research Institute of Multidisciplinary Science, Beijing Institute of Technology, Beijing 100081, China
e-mail: chunlizhu@bit.edu.cn

G.-Z. Zheng, J. Zhang
School of Physics, Shaanxi Normal University, Xi'an 710119, China

Y.-C. Lin
The Institute of Scientific and Industrial Research, Osaka University, Osaka 567-0047, Japan

D.-Z. Zheng, J.-D. Zhou
Advanced Research Institute of Multidisciplinary Science, Beijing Institute of Technology, Beijing 100081, China

1 Introduction

Two-dimensional (2D) transition metal disulfides (TMDs) have obtained extensive attention due to their atomically thin thickness, wide tunable band gap and high carrier mobility [1–5]. Among them, Mo- and W-based TMDs are ideal candidates for the next generation photoelectric devices for their excellent physical properties, such as high Young's modulus, superconductivity and nonlinear Hall effect [6–8]. Specifically, the physical properties of monolayer MoS$_2$ with direct gap have been thoroughly investigated [9–11]. Compared with monolayer MoS$_2$, bilayer MoS$_2$ displays higher density states and carrier mobility, which has great potential in the realization of high-performance electronic devices [12–15].

However, the electronic structure of bilayer MoS$_2$ is sensitive to the stacking configuration between adjacent layers [11]. The most stable stacking configurations for MoS$_2$ are hexagonal 2H and rhombohedral 3R due to their favorable energy, which can be directly realized by chemical vapor deposition (CVD) process [16, 17]. For the 2H MoS$_2$, the Mo atoms are arranged vertically with the sulfur atoms in the adjacent layers, with an AB stacking order, resulting

centrosymmetry (non-centrosymmetry) in the even (odd) layers [18, 19]. In contrast, 3R type exhibits AA stacking order of adjacent layers in same crystalline orientation, and the second layer shows in-plane shift relative to the first layer [20, 21]. Since there is no inverse symmetry, the 3R stacking has parallel in-plane nonlinear dipoles [22]. Therefore, 3R MoS_2 always exhibits independent SHG signal of the layer thickness.

Previous studies have shown that tuning the interlayer interaction can bring about many exotic physical phenomena, which may be inaccessible in monolayer TMDs [22–27]. However, folding, high pressure, and twisting methods are affected by complex manufacturing processes and low yields, and it is difficult to meet the current device requirements [28–30]. Different from the above methods, substitution doping through CVD, as one of the most effective and technologically mature methods in silica-based manufacturing processes, has been widely applied to tune the physical properties of TMDs [31–33]. Therefore, this work reports the synthesis of bilayer V-doped MoS_2 with 2H and 3R phase via salt-assisted CVD method. The inverse symmetry of the bilayer 3R stacking V-doped MoS_2 is broken, showing a significant SHG signal. Additionally, combining electrical measurements and DFT calculations, it is found that the 6.2% higher effective mobility of 3R over the 2H stacking is attributed to the stronger interlayer coupling. This work provides the way for tuning the optical and electrical properties of 2D TMDs through doping engineering and contribute to the future research of optoelectronic devices.

2 Experimental

2.1 CVD synthesis of V-doped MoS_2

V-doped MoS_2 sheets were synthesized by atmospheric pressure CVD method. MoO_3 (Aladdin, 99.999%), V_2O_5 (Aldrich, 99.99%) and S powder (Aladdin, 99.95%) were purchased as source precursors. A powder mixture of 1 mg KI, 3 mg MoO_3 and 3 mg V_2O_5 in an aluminium oxide boat was placed in the center of the quartz tube. 100 mg S powder was placed at the upstream side of the furnace. The SiO_2/Si substrate was placed face down on the boat with ∼1 cm distance. The furnace was heated to 800 °C with a ramp rate of 35 °C·min^{-1}. The carrier gas was Ar:H_2 = 95:5 ml·min^{-1}. After holding for 5 min at the growth temperature, the furnace was decreased to room temperature naturally.

2.2 Characterization

Optical imaging was taken by ZEISS Primotech microscope. Atomic force microscopy (AFM) experiments were performed by Bruker Dimension Icon system. The element composition was analyzed by X-ray photoelectron spectroscopy (XPS, Thermo Scientific K-Alpha). Raman and SHG spectra/mapping characterizations were carried out with WITEC alpha 300R Raman system. Scanning transmission electron microscopy (STEM) imaging was performed by FEI Themis system.

2.3 Device fabrication and measurements

The V-doped MoS_2 devices were fabricated on the SiO_2/Si (285 nm) substrate via the standard electron-beam lithography and lift-off process, and then the contact metal of Cr/Au (5/50 nm) were deposited by thermal evaporation. The electrical and photoelectric characteristics were measured by using KEYSIGHT B1500A source-meter unit. The photoresponse of the devices were performed under 532-nm light irradiation.

2.4 Theoretical calculations

DFT calculations were performed with the VASP suite. We used projector augmented-wave pseudopotentials within the Perdew–Burke–Ernzerhof approximation for the exchange–correlation functional and the kinetic energy cutoff was fixed to 450 eV. The 2H and 3R stacking bilayer V-doped MoS_2 geometry was relaxed until all forces less than 0.1 eV·nm^{-1}. For the electronic structure calculations, the lattice constants of 2H stacking V-MoS_2 (a = 0.3196 nm) and 3R stacking V-MoS_2 (a = 0.3180 nm) were obtained through full relaxation with a total energy tolerance of 1×10^{-6} eV and a Γ-centered k-grid of $6 \times 6 \times 1$. The above calculations are carried out in the consideration of spin-dependent interactions.

3 Results and discussion

The bilayer V-doped MoS_2 sheets were synthesized by the salt-assisted CVD method, as displayed in Fig. 1a. Briefly, the mixed MoO_3, V_2O_5 and KI powder were served as precursors in the center of the heating zone, while the S precursor was placed in the upstream. More detailed information can be found in the Experimental section. The atomic configurations of 2H and 3R stacking V-doped MoS_2 crystal is schematically shown in the right side of Fig. 1a. The 2H stacking (60°) displays vertically alignment, while 3R stacking (0°) shows a staggered arrangement with an obvious in-plane shift. In order to confirm the existence of V, XPS characterization of the 2D V-doped MoS_2 sheets were collected. The fine spectrum of V 2p, Mo 3d, S 2p state and full spectrum are shown in Fig. 1b–e, respectively. As shown in Fig. 1b, two obvious
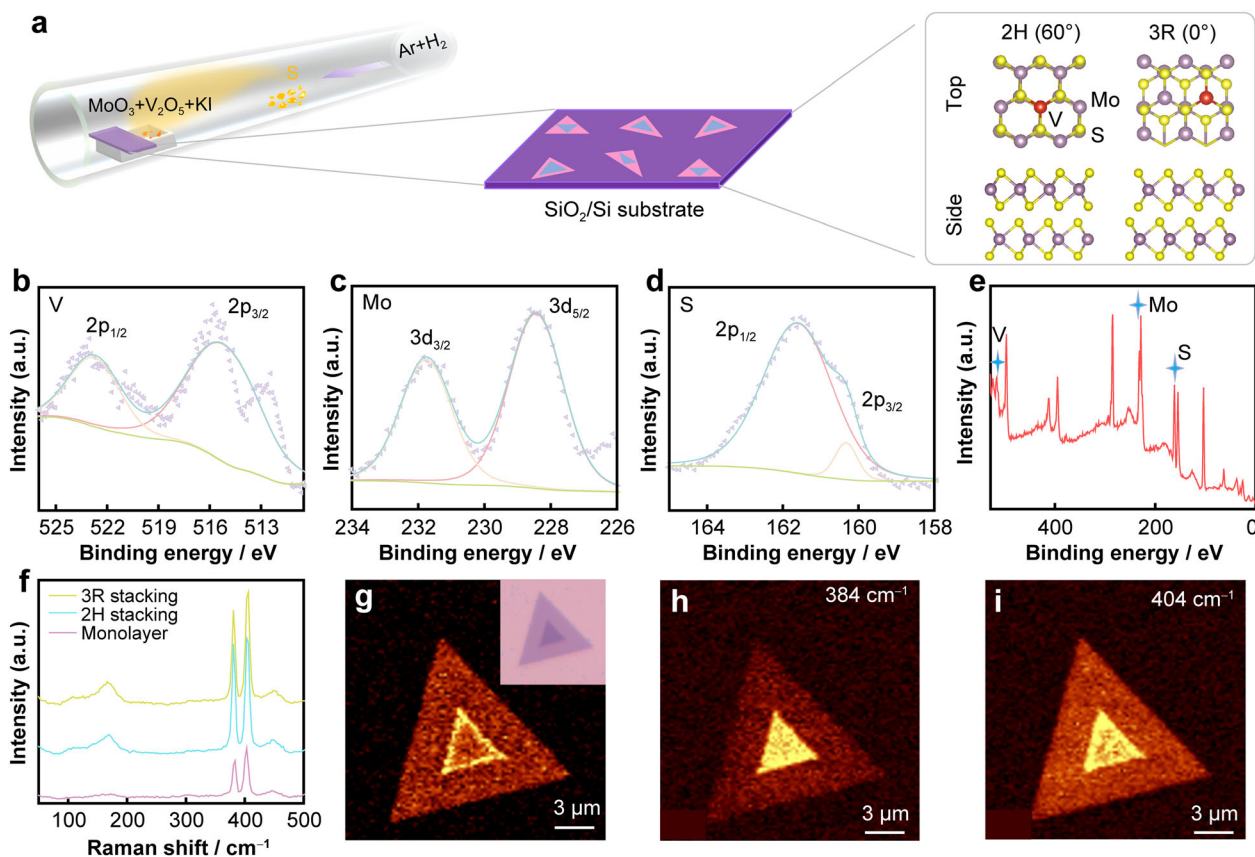
Fig. 1 a Synthetic schematic diagram and atomic stacking configuration of V-doped MoS$_2$; **b–e** XPS fine spectra of V 2p, Mo 3d, S 2p orbitals and full spectrum, respectively; **f** Raman spectra of monolayer MoS$_2$ and V-doped bilayer MoS$_2$ (2H and 3R stacking) sheets with V doping; **g–i** Raman intensity mapping images at 100–200, 384 and 404 cm^{-1}, respectively, and (inset in **g**) corresponding optical image

characteristic peaks are located at about 523.7 eV ($2p_{1/2}$) and 515.9 eV ($2p_{3/2}$), which is consistent with the chemical state of V^{4+}, demonstrating the successful replacement of V atoms in MoS$_2$ lattice. The experimental result presented by lilac scatters is rough, indicating a low concentration of V-doped MoS$_2$ sheets. The peaks of Mo 3d core level state are located at about 231.6 and 228.4 eV, corresponding to Mo $3d_{3/2}$ and Mo $3d_{5/2}$, respectively. As for the spectra of S 2p core level binding energy, the two peaks are located at 161.7 and 160.5 eV, corresponding to S $2p_{1/2}$ and S $2p_{3/2}$, respectively. Compared to the previously reported pure MoS$_2$, the bonding states of S and Mo elements in V-doped MoS$_2$ exhibit a small shift, which may be caused by V doping in the MoS$_2$. Furthermore, Raman spectroscopy was used to study the V-doping effect of the MoS$_2$ structure and electronic properties. Figure 1f shows Raman spectra of monolayer and bilayer MoS$_2$ (2H and 3R phases) sheets with V doping (Fig. S1). Both the monolayer and bilayer MoS$_2$ display peaks at about 384 and 404 cm^{-1}, corresponding to the in-plane vibrations of Mo and S atoms (E_{2g}^1) and the out-of-plane vibrations of S atoms (A_{1g}), respectively. However, after doping with V, additional

peaks appear between 100 and 200 cm^{-1} in both monolayer and bilayer MoS$_2$. The V-doped 2H and 3R-stacking bilayer MoS$_2$ exhibits a close Raman spectra. These new Raman peaks may be associated with the reduction of the host lattice symmetry since the V dopant can induce disorder in the pristine MoS$_2$. Figure 1g-i shows Raman mapping of bilayer 3R MoS$_2$ with V doping corresponding to the above peaks, which is further proved the successful V doping of MoS$_2$.

To precisely assess the crystalline quality, high-angle annular dark-field scanning transmission electron microscopy (HAADF-STEM) and selected area electron diffraction (SAED) were employed to explore the atomic structure of the as-synthesized V-doped MoS$_2$ sample. Figure 2a shows the atomic-scale HAADF-STEM image of the monolayer V-doped MoS$_2$. It is known that the intensity in HAADF-STEM image is approximately proportional to the atomic number Z value, thus the brightness of V atoms is lower than that of Mo atoms. The intensity profile of five metal sites highlighted by yellow rectangle is clearly seen that the intensity of the third metal site is weaker than that of other four sites, confirming the
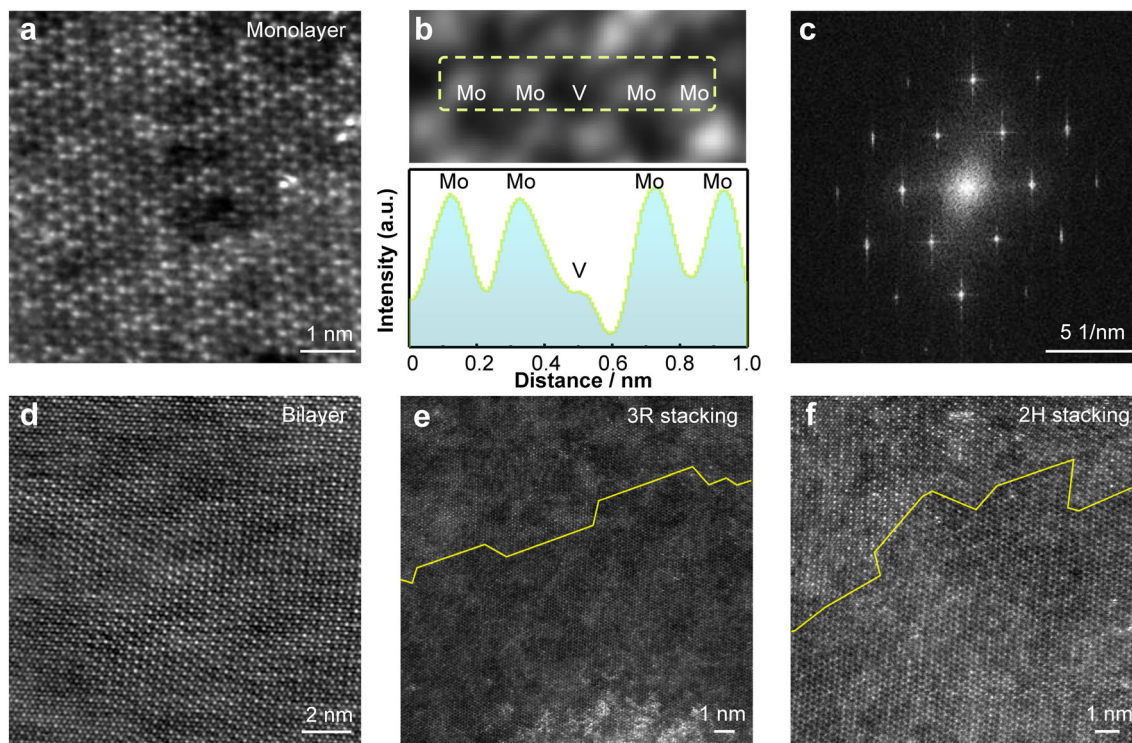
Fig. 2 a HAADF-STEM image of monolayer V-doped MoS$_2$; **b** enlarged enlarged STEM image and corresponding atomic intensity profile along highlighted yellow dashed region; **c** SAED pattern of monolayer V-doped MoS$_2$; **d–f** HAADF-STEM images of bilayer, 3R and 2H V-doped MoS$_2$, respectively

successful substitution of V atom. SAED pattern (Fig. 2c) exhibits hexagonally arranged diffraction spots, indicating no lattice mismatch generation after the doping of V atoms in MoS$_2$. Furthermore, bilayer, 3R stacking and 2H stacking V-doped MoS$_2$ were also detected by HAADF-STEM, as displayed in Fig. 2d–f. The stacking configuration transition can be directly identified from the obvious atomic contrast, which is consistent with corresponding atomic model.

To distinguish the effect of V substitution and stacking order, SHG of V-doped MoS$_2$ is further explored. Figure 3a is a schematic diagram of SHG process under a pump excitation (λ = 1064 nm). The uniform sample with monolayer and bilayer V-doped MoS$_2$ was selected (Fig. 3b), the SHG mapping intensity shows a sharp contrast between 2H and 3R stacking, as displayed in Fig. 3c. The SHG mapping intensity of 3R stacking is increased, while 2H stacking is decreased comparing with monolayer sample (Fig. S2). The corresponding single SHG spectrum all emerged at 532 nm with distinct intensity value (Fig. 3d), which is consistent with the mapping image. It is worth noting that the bilayer 2H V-doped MoS$_2$ also generates a weak SHG signal, indicating a break of inverse symmetry. This may be caused by slightly lattice strain from V substitution. Additionally, the polarization angle-dependent SHG was carried out to explore the crystal

structure. The bilayer 3R V-doped MoS$_2$ under perpendicular and parallel laser both present typical six-fold symmetric patterns (Fig. 3e, f), illustrating the hexagonal structure of V-doped MoS$_2$.

We also fabricated field-effect transistors (FETs) to demonstrate the performance of the 2H and 3R stacking bilayer V-doped MoS$_2$, as illustrated in Fig. 4a. The transistor consists of Cr/Au contact metal, 2H/3R bilayer V-MoS$_2$ channel material, and 285-nm SiO$_2$ dielectric. The channel width is 5 μm for all the FET devices. The output curves of 2H and 3R stacking V-MoS$_2$ are shown in Fig. 4b. The 3R stacking V-MoS$_2$ FET demonstrated a significantly higher on-state current than 2H stacking. The corresponding transfer curves of 2H and 3R stacking V-MoS$_2$ are shown in Fig. 4c. The mobility (μ) was obtained using the equation $\mu = g_{m}L_{ch}/WC_{ox}V_{ds}$, where g_{m}, L_{ch}, W, C_{ox}, and V_{ds} are the transconductance, channel length, channel width, gate oxide capacitance per unit area of the dielectric layer, and drain voltage, respectively. The calculated μ values for the 2H and 3R bilayer V-MoS$_2$ FETs were 25.6 and 31.8 cm$^2 \cdot$V$^{-1} \cdot$s^{-1}, respectively. The photodetection performance of 2H and 3R stacking bilayer V-doped MoS$_2$ were further explored as shown in Fig. 4d, e. The 3R stacking V-doped MoS$_2$ exhibits a higher photocurrent than that of 2H stacking V-MoS$_2$ under various power density. The photocurrent (I_{ph}) exhibits an
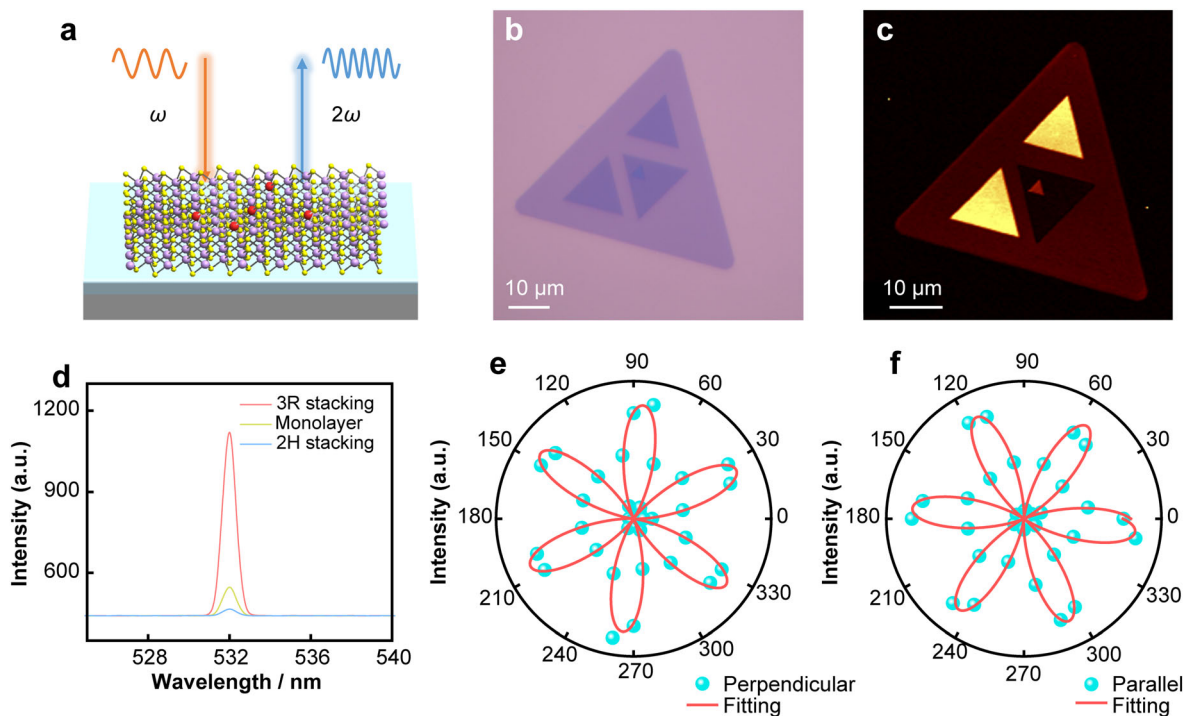
Fig. 3 **a** Schematic diagram of SHG; **b** optical image of V-doped MoS$_2$ with 3R and 2H stacking; **c** SHG intensity mapping of V-doped MoS$_2$ with 3R and 2H stacking at 532 nm; **d** stacking configuration dependent SHG of monolayer, 3R and 2H V-doped MoS$_2$; **e, f** Angular-dependent SHG intensity of V-doped 3R MoS$_2$
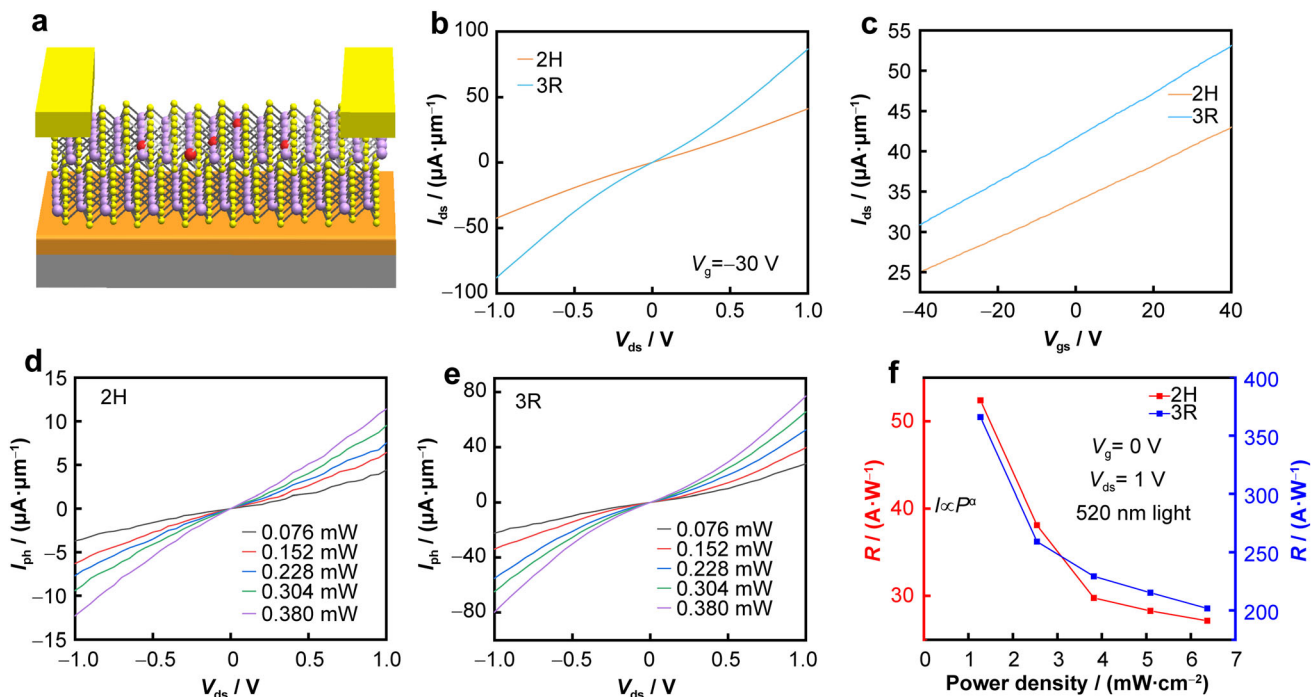

Fig. 4 **a** Schematic illustration of bilayer V-doped MoS$_2$ FETs; **b** output curves of 2H and 3R stacking bilayer V-doped MoS$_2$ FETs; **c** transfer curves of 2H and 3R stacking bilayer V-doped MoS$_2$ FETs; **d, e** output curves of 2H and 3R stacking bilayer V-doped MoS$_2$ FETs at different power densities; **f** responsivity (2H and 3R stacking bilayer V-doped MoS$_2$ FETs) as a function of different power densities under zero bias

exponential dependence on the incident power density (P), $I_{ph} = P^\alpha$ (α is fitted exponent), which is 0.15 for 2H and 0.4 for 3R stacking V-doped MoS_2. Furthermore, the key performance metrics for photodetector were evaluated, including responsivity (R), detectivity (D^*), and external quantum efficiency (EQE). R is defined as $R = I_{ph}/(P \times A)$, where I_{ph} is the photocurrent, P is the power density, and A is the channel area. The relationship between R and P for 2H and 3R stacking V-MoS_2 is shown in Fig. 4f. The R values are 52.4 and 366 $A \cdot W^{-1}$ for 2H and 3R stacking V-MoS_2 at 1.28 $mW \cdot cm^{-2}$, respectively. The corresponding D^* and EQE of 2H and 3R stacking V-MoS_2 are displayed in Fig. S3. The highest D^* value of 2H and 3R stacking V-doped MoS_2 reaches 3.7×10^7 and 2.53×10^8 J, respectively. The EQE values for 2H and 3R stacking V-MoS_2 are 125.7 and 866.4, respectively. The above results indicate that 3R stacking V-doped MoS_2 exhibits better conductance and carrier mobility than that of 2H stacking V-doped MoS_2, which substantially enhances the electrical and photodetector performance.

To precisely understanding the physical mechanism of interlayer coupling enhanced by V-doped MoS_2, DFT calculations were performed on 2H and 3R stacking bilayer V-doped MoS_2. The projected band structure and density of states (DOS) for these systems are shown in Fig. 5a, b, where Fermi level is defined as the zero energy level. For both 2H and 3R stacking bilayer V-doped MoS_2, the total

DOS at the Fermi level is non-zero with four energy bands crossing the Fermi level, which is attributed to the contribution from the doped V atoms. The band gaps of 2H and 3R stacking bilayer V-MoS_2 are much smaller than the reported band gap values of pure MoS_2 and monolayer V-MoS_2 (Fig. S4). This is consistent with the metal-like behavior in the previous electrical properties. Additionally, the DOS of 2H and 3R stacking bilayer V-doped MoS_2 can be divided into two parts from -1 to 2 eV. The V 3d orbital electrons mainly contribute to the part beside conduction band minimum, while both V 3d and Mo 4d orbital electrons primarily contribute to the part beside the valence band maximum. The detailed DOS information of 2H and 3R stacking bilayer V-doped MoS_2 is shown in Fig. S5.

The synergistically interaction mechanism of doping and stacking configuration of 2H and 3R stacking bilayer V-doped MoS_2 was further explored through differential charge density. The differential charge density from middle to upper surface of the stacking layer was plotted, as shown in Fig. 5c, d. Compared to 2H stacking, 3R stacking exhibits a richer distribution of interlayer charge density. Additionally, the charge density changes along the perpendicular direction are displayed in Fig. 5e, f. The 3R stacking bilayer V-doped MoS_2 electron clouds tend to overlap with adjacent layers, indicating stronger coupling, while there is almost no electron accumulation between 2H stacking bilayer V-doped MoS_2. This phenomenon is
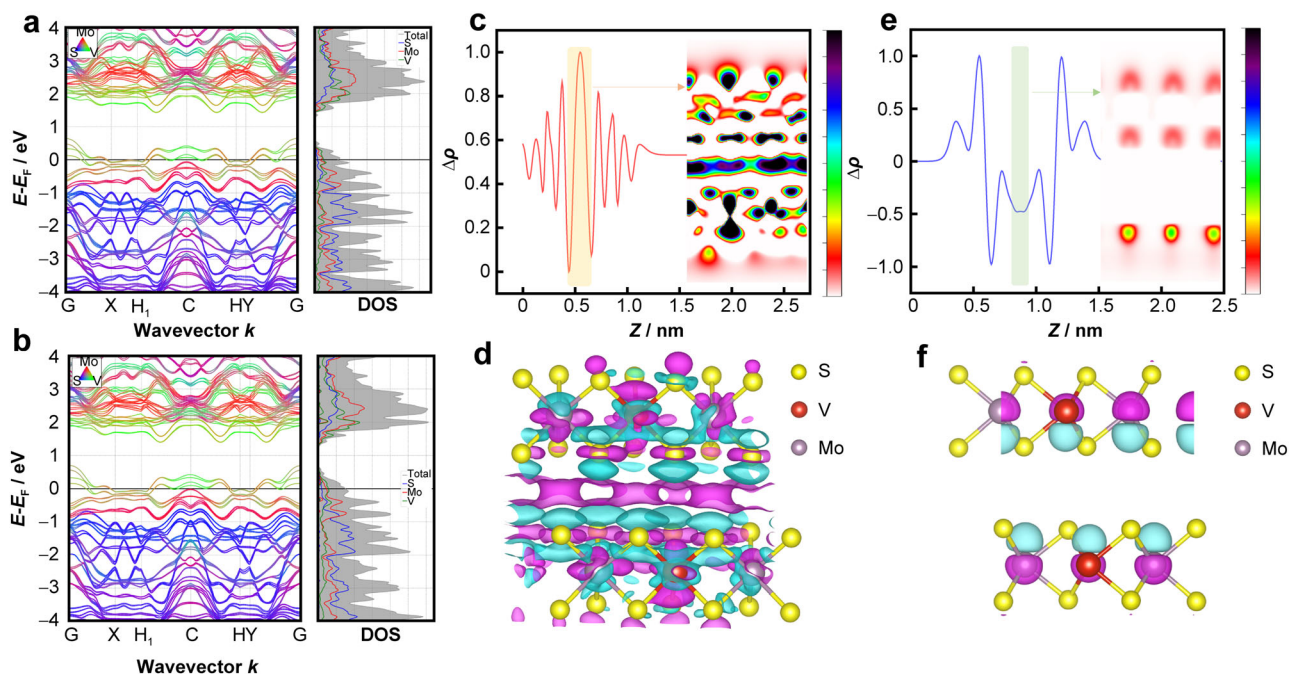

Fig. 5 **a, b** DFT calculations for projected band energy of 2H and 3R stacking bilayer V-doped MoS_2; **c, e** planar-average charge density difference of 2H and 3R stacking bilayer V-doped MoS_2 along c-axis, and (insets) charge density distribution diagrams in middle interlayer of 2H and 3R stacking bilayer V-doped MoS_2; **d, f** schematic diagram of differential charge density for 2H and 3R stacking bilayer V-doped MoS_2, where purple area represents gained electrons, and blue area represents lost electrons

attributed to the symmetry difference between 2H and 3R-configuration, which is consistent with the SHG results.

4 Conclusion

In summary, we have implemented a comprehensive experimental and theoretical investigation of the optical and electrical properties of CVD grown 2H and 3R stacking bilayer V-doped MoS₂. The 3R stacking of V-doped MoS₂ displays higher carrier mobility due to a stronger interlayer coupling compared to the 2H stacking configuration, which agrees with the DFT calculations. Our work shows that the synergistic regulation strategy of doping and different stacking configurations not only offers the possibility to extend second-order nonlinear optical materials, but also provides a promising way to achieve high-performance photodetectors.

Declarations

Conflict of interests The authors declare that they have no conflict of interest.

References

[1] Peng J, Liu Y, Luo X, Wu JJ, Lin Y, Guo YQ, Zhao JY, Wu XJ, Wu CZ, Xie Y. High phase purity of large-sized 1T'-MoS₂ monolayers with 2D superconductivity. Adv Mater. 2019; 31(19):e1900568. https://doi.org/10.1002/adma.201900568.

[2] Liu LN, Sun L, Zheng JY, Xing L, Gu L, Wu JX, Wu LY, Ye M, Liu XZ, Wang Q, Hou SY, Jiang XW, Xie LM, Lu PF, Jiao LY. Phase-selective synthesis of 1T' MoS₂ monolayers and heterophase bilayers. Nat Mater. 2018;17(12):1108. https://doi.org/10.1038/s41563-018-0187-1.

[3] Acerce M, Voiry D, Chhowalla M. Metallic 1T phase MoS₂ nanosheets as supercapacitor electrode materials. Nat Nanotechnol. 2015;10(4):313. https://doi.org/10.1038/nnano.2015.40.

[4] Cheon Y, Lim S, Kim K, Cheong H. Structural phase transition and interlayer coupling in few-layer 1T' and Td MoTe₂. ACS Nano. 2021;15(2):2962. https://doi.org/10.1021/acsnano.0c09162.

[5] Yu YF, Nam G, He QY, Wu XJ, Zhang K, Yang ZZ, Chen JZ, Ma QL, Zhao MT, Liu ZQ, Ran FR, Wang XZ, Li H, Huang X, Li B, Xiong QH, Zhang Q, Liu Z, Gu L, Du YH, Huang W, Zhang H. High phase-purity 1T'-MoS₂- and 1T'-MoSe₂-layered crystals. Nat Chem. 2018;10(6):638. https://doi.org/10.1038/s41557-018-0035-6.

[6] Fang YQ, Pan J, He JQ, Luo RC, Wang D, Che XL, Bu KJ, Zhao W, Liu P, Mu G, Zhang H, Lin TQ, Huang FQ. Structure re-determination and superconductivity observation of bulk 1T MoS₂. Angew Chem Int Ed. 2018;57(5):1232. https://doi.org/10.1002/anie.201710512.

[7] Wang Y, Xiao J, Zhu HY, Li Y, Alsaid Y, Fong KY, Zhou Y, Wang SQ, Shi W, Wang Y, Zettl A, Reed EJ, Zhang X. Structural phase transition in monolayer MoTe₂ driven by electrostatic doping. Nature. 2017;550(7677):487. https://doi.org/10.1038/nature24043.

[8] Zhang LF, Nan H, Zhang XM, Liang QF, Du AJ, Ni ZH, Gu XF, Ostrikov K, Xiao S. 2D atomic crystal molecular superlattices by soft plasma intercalation. Nat Commun. 2020;11(1):5960. https://doi.org/10.1038/s41467-020-19766-x.

[9] Suh J, Tan T, Zhao WJ, Park J, Lin DY, Park TE, Kim J, Jin CH, Saigal N, Ghosh S, Wong ZM, Chen YB, Wang F, Walukiewicz W, Eda G, Wu JQ. Reconfiguring crystal and electronic structures of MoS₂ by substitutional doping. Nat Commun. 2018; 9(1):199. https://doi.org/10.1038/s41467-017-02631-9.

[10] Shi ZT, Zhao HB, Chen XQ, Wu GM, Wei F, Tu HL. Chemical vapor deposition growth and transport properties of MoS₂-2H thin layers using molybdenum and sulfur as precursors. Rare Met. 2022;41(10):3574. https://doi.org/10.1007/s12598-015-0599-x.

[11] Regan EC, Wang D, Paik EY, Zeng YX, Zhang L, Zhu JH, MacDonald AH, Deng H, Wang F. Emerging exciton physics in transition metal dichalcogenide heterobilayers. Nat Rev Mater. 2022;7(10):778. https://doi.org/10.1038/s41578-022-00440-1.

[12] Liu L, Li T, Ma L, Li WS, Gao S, Sun WJ, Dong RK, Zou XL, Fan DX, Shao LW, Gu CY, Dai NX, Yu ZH, Chen XQ, Tu XC, Nie YF, Wang P, Wang JL, Shi Y, Wang XR. Uniform nucleation and epitaxy of bilayer molybdenum disulfide on sapphire. Nature. 2022;605(7908):69. https://doi.org/10.1038/s41586-022-04523-5.

[13] Cheng YH, Chen J, Che HN, Ao YH, Liu B. Ultrafast photocatalytic degradation of nitenpyram by 2D ultrathin Bi₂WO₆: mechanism, pathways and environmental factors. Rare Met. 2022;41(7):2439. https://doi.org/10.1007/s12598-022-01984-5.

[14] Li TT, Guo W, Ma L, Li WS, Yu ZH, Han Z, Gao S, Liu L, Fan DX, Wang ZX, Yang Y, Lin WY, Luo ZZ, Chen XQ, Dai NX, Tu XC, Pan DF, Yao YG, Wang P, Nie YF, Wang JL, Shi Y, Wang XR. Epitaxial growth of wafer-scale molybdenum disulfide semiconductor single crystals on sapphire. Nat Nanotechnol. 2021;16(11):1201. https://doi.org/10.1038/s41565-021-00963-8.

[15] Chen ZZ, Hou JG, Zhou J, Huang P, Wang HQ, Xu CX. Carbon shell coated hollow NiCoSex composite as high-performance anode for lithium storage. Rare Met. 2021;40(11):3185. https://doi.org/10.1007/s12598-021-01748-7.

[16] Liu KH, Zhang L, Cao T, Jin CH, Qiu DN, Zhou Q, Zettl A, Yang PD, Louie SG, Wang F. Evolution of interlayer coupling in twisted molybdenum disulfide bilayers. Nat Commun. 2014; 5(1):4966. https://doi.org/10.1038/ncomms5966.

[17] Song JG, Ryu G, Lee SJ, Sim S, Lee CW, Choi T, Jung H, Kim Y, Lee Z, Myoung JM, Dussarrat C, Matras CL, Park J, Choi H, Kim H. Controllable synthesis of molybdenum tungsten disulfide alloy for vertically composition-controlled multilayer. Nat Commun. 2015;6(1):7817. https://doi.org/10.1038/ncomms8817.

[18] Zeng ZXS, Sun X, Zhang DL, Zheng WH, Fan XP, He M, Xu T, Sun LT, Wang X, Pan AL. Controlled vapor growth and nonlinear optical applications of large-area 3R phase WS₂ and WSe₂ atomic layers. Adv Funct Mater. 2019;29(11):1806874. https://doi.org/10.1002/adfm.201806874.

[19] Song Y, Tian R, Yang JL, Yin R, Zhao JL, Gan XT. Second harmonic generation in atomically thin MoTe₂. Adv Opt Mater. 2018;6(17):1701334. https://doi.org/10.1002/adom.201701334.

[20] Liang LB, Zhang J, Sumpter BG, Tan QH, Tan PH, Meunier V. Low-frequency shear and layer-breathing modes in raman scattering of two-dimensional materials. ACS Nano. 2017; 11(12):11777. https://doi.org/10.1021/acsnano.7b06551.

[21] Zhang JS, Yang A, Wu X, de Groep JV, Tang P, Li SR, Liu BF, Shi FF, Wan JY, Li QT, Sun YM, Lu ZY, Zheng XL, Zhou GM, Wu CL, Zhang SC, Brongersma ML, Li J, Cui Y. Reversible and selective ion intercalation through the top surface of few-layer MoS_2. Nat Commun. 2018;9(1):5289. https://doi.org/10.1038/s41467-018-07710-z.

[22] Wu WZ, Wang L, Li YL, Zhang F, Lin L, Niu SM, Chenet D, Zhang X, Hao YF, Heinz TF, Hone J, Wang ZL. Piezoelectricity of single-atomic-layer MoS_2 for energy conversion and piezotronics. Nature. 2014;514(7523):470. https://doi.org/10.1038/nature13792.

[23] Zhao XX, Song P, Wang CC, Riis-Jensen AC, Fu W, Deng Y, Wan DY, Kang LX, Ning SC, Dan JD, Venkatesan T, Liu Z, Zhou W, Thygesen KS, Luo X, Pennycook SJ, Loh KP. Engineering covalently bonded 2D layered materials by self-intercalation. Nature. 2020;581(7807):171. https://doi.org/10.1038/s41586-020-2241-9.

[24] Wang XW, Hou LF, Huang W, Ren XB, Ji W, Jin CH. Mass transport induced structural evolution and healing of sulfur vacancy lines and Mo chain in monolayer MoS_2. Rare Met. 2022;41(1):333. https://doi.org/10.1007/s12598-021-01758-5.

[25] Cui SS, Liu X, Shi YB, Ding MY, Yang XF. Construction of atomic-level charge transfer channel in $Bi_{12}O_{17}Cl_2$/MXene heterojunctions for improved visible-light photocatalytic performance. Rare Met. 2022;41(7):2405. https://doi.org/10.1007/s12598-022-02011-3.

[26] Deng QX, Li X, Si HY, Hong JH, Wang SY, Feng QL, Hu CX, Wang SS, Zhang HL, Suenaga K, Xu H. Strong band bowing effects and distinctive optoelectronic properties of 2H and 1T' phase-tunable $Mo_xRe_{1-x}S_2$ alloys. Adv Funct Mater. 2020;30(34):2003264. https://doi.org/10.1002/adfm.202003264.

[27] Zeng ZY, Yin Z, Huang X, Li H, He QY, Lu G, Boey F, Zhang H. Single-layer semiconducting nanosheets: high-yield preparation and device fabrication. Angew Chem Int Ed Engl. 2011;50(47):11093. https://doi.org/10.1002/anie.201106004.

[28] Cai ZY, Shen T, Zhu Q, Feng SM, Yu QM, Liu JM, Tang L, Zhao Y, Wang JW, Liu BL, Cheng HM. Dual-additive assisted chemical vapor deposition for the growth of Mn-doped 2D MoS_2 with tunable electronic properties. Small. 2020;16(15): e1903181. https://doi.org/10.1002/smll.201903181.

[29] Wu YC, Wang J, Li YB, Zhou JW, Wang BY, Yang AK, Wang LW, Hwang HY, Cui Y. Observation of an intermediate state during lithium intercalation of twisted bilayer MoS_2. Nat Commun. 2022;13(1):3008. https://doi.org/10.1038/s41467-022-30516-z.

[30] Song TC, Sun QC, Anderson E, Wang C, Qian JM, Taniguchi T, Watanabe K, McGuire MA, Stöhr R, Xiao D, Cao T, Wrachtrup J, Xu XD. Direct visualization of magnetic domains and moiré magnetism in twisted 2D magnets. Science. 2021;374(6571): 1140. https://doi.org/10.1126/science.abj7478.

[31] Empante TA, Zhou Y, Klee V, Nguyen AE, Lu IH, Valentin MD, Alvillar SAN, Preciado E, Berges AJ, Merida CS, Gomez M, Bobek S, Isarraraz M, Reed EJ, Bartels L. Chemical vapor deposition growth of few-layer $MoTe_2$ in the 2H, 1T', and 1T phases: tunable properties of $MoTe_2$ films. ACS Nano. 2017; 11(1):900. https://doi.org/10.1021/acsnano.6b07499.

[32] Zhang LL, Wang Z, Zhang JW, Chen B, Liang ZM, Quan XN, Dai YD, Huang JF, Wang YT, Liang SJ, Long MS, Si MS, Miao F, Peng Y. Quasi-continuous tuning of carrier polarity in monolayered molybdenum dichalcogenides through substitutional vanadium doping. Adv Funct Mater. 2022;32(46): 2204760. https://doi.org/10.1002/adfm.202204760.

[33] Seo J, Son E, Kim J, Kim SW, Baik JM, Park H. Controllable substitutional vanadium doping in wafer-scale molybdenum disulfide films. Nano Res. 2023;16(2):3415. https://doi.org/10.1007/s12274-022-4945-7.